Available online at www.sciencedirect.com
SCIENCE DIRECT®
International Journal of Heat and Fluid Flow 26 (2005) 56–70
International Journal of HEAT AND FLUID FLOW
www.elsevier.com/locate/ijhff

Numerical and experimental investigations on supersonic ejectors

Y. Bartosiewicz [a,*], Zine Aidoun [a], P. Desevaux [b], Yves Mercadier [c]

[a] CETC-Varennes, Natural Resources Canada, P.O. Box 4800, 1615 Boulevard Lionel-Boulet, Varennes (Qc.), Canada J3X 1S6
[b] CREST-UMR 6000, IGE-Parc Technologique, 90000 Belfort, France
[c] THERMAUS, Université de Sherbrooke, 2500 Boul. Université, Sherbrooke (Qc.), Canada J1K2R1

Received 9 January 2004; accepted 13 July 2004
Available online 11 September 2004

Abstract

Supersonic ejectors are widely used in a range of applications such as aerospace, propulsion and refrigeration. The primary interest of this study is to set up a reliable hydrodynamics model of a supersonic ejector, which may be extended to refrigeration applications.

The first part of this work evaluated the performance of six well-known turbulence models for the study of supersonic ejectors. The validation concentrated on the shock location, shock strength and the average pressure recovery prediction. Axial pressure measurements with a capillary probe performed previously [Int. J. Turbo Jet Engines 19 (2002) 71; Conference Proc., 10th Int. Symp. Flow Visuzlization, Kyoto, Japan, 2002], were compared with numerical simulations while laser tomography pictures were used to evaluate the non-mixing length. The capillary probe has been included in the numerical model and the non-mixing length has been numerically evaluated by including an additional transport equation for a passive scalar, which acted as an ideal colorant in the flow. At this point, the results show that the *k*–omega–sst model agrees best with experiments.

In the second part, the tested model was used to reproduce the different operation modes of a supersonic ejector, ranging from on-design point to off-design. In this respect, CFD turned out to be an efficient diagnosis tool of ejector analysis (mixing, flow separation), for design, and performance optimization (optimum entrainment and recompression ratios).

Keywords: Shock waves; Turbulence modeling; Pressure measurements; Supersonic ejector; Refrigeration; Shock-boundary layer interaction; On–off-design

1. Introduction

Supersonic ejectors are simple mechanical components (Fig. 1), which generally allow to perform the mixing and/or the recompression of two fluid streams. The fluid with the highest total energy is the motive or primary stream (stream 1 in Fig. 1), while the other, with the lowest total energy (stream 2) is the secondary or the induced stream. Operation of such systems is also quite simple: the motive stream (high pressure and temperature) flows through a convergent divergent nozzle to reach supersonic velocity. By an entrainment-induced effect, the secondary stream is drawn into the flow and accelerated. Mixing, and recompression of the resulting stream then occurs in a mixing chamber, where complex interactions take place between the mixing layer and shocks. In other words, there is a mechanical energy transfer from the highest to the lowest energy level, with a mixing pressure lying between the motive or driving pressure and the induction pressure.

Ejectors for compressible fluids are not new and have been known for a long time. These are mechanical components that have found many applications in engineer-

* Corresponding author. Tel.: +1 450 652 0352.
E-mail addresses: ybartosi@rncan.gc.ca (Y. Bartosiewicz), zaidoun@rncan.gc.ca (Z. Aidoun), philippe.desevaux@univ-fcomte.fr (P. Desevaux), yves.mercadier@usherbrooke.ca (Y. Mercadier).

0142-727X/$ - see front matter © 2004 Elsevier Inc. All rights reserved.
doi:10.1016/j.ijheatfluidflow.2004.07.003

Nomenclature

ρ	density	Γ	passive scalar
u_i	velocity	m	mass flow rate
u_i'	fluctuating velocity		
P	pressure	*Subscripts*	
τ_{ij}	stress tensor	1	primary inlet
α	thermal conductivity	2	secondary inlet
μ	dynamic viscosity	3	outlet
E	total energy	eff	effective
y^+	wall coordinate	i,j,k	space components
k	turbulent kinetic energy		

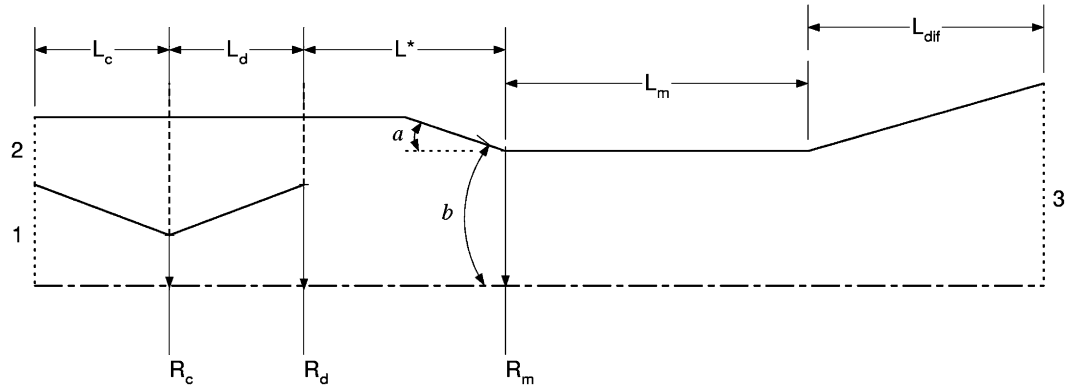

Fig. 1. Ejector geometry.

ing. In aerospace engineering, they are used for altitude testing of a propulsion system by reducing the pressure of a test chamber (Roshke et al., 1962). The pumping effect is also used to mix exhaust gases with fresh air in order to reduce the thermal signature (Zhou et al., 2000). A most-researched area is the ejector application for thrust augmentation on aircraft propulsion systems (Alperin and Wu, 1983a; Alperin and Wu, 1983b).

Our primary interest in this paper is the use of supersonic ejectors in refrigeration. In view of the numerous publications available on this subject, it is perhaps one of the most important application areas for ejectors. A good overview of the different applications in this field may be found in the review article by Sun and Eames (1995). Ejectors may either totally replace mechanical compressors or simply be used for cycle optimization (Aidoun and Ouzzane, in press). In this particular case, they have become the focus of renewed interest for many scientists, in an attempt to develop energy efficient and environment-friendly techniques, in response to current practices, responsible for environmental damages such as ozone depletion or global warming.

Many theoretical and experimental studies were performed in order to understand not only the fundamental mechanisms in terms of fluid dynamics and heat transfer, but also ejector operational behaviour. Nevertheless, most of them relied on semi-empirical or one-dimensional models. Keenan and Newman (1946) and Keenan et al. (1950) set the first step by their 1-D model for air with constant area mixing and later with the concept of constant pressure mixing still used today. Munday and Bagster (1977) introduced the fictive throat to explain the characteristic ejector maximum capacity limitations. This kind of models was later applied to refrigerants and the fictive throat was placed in the constant area zone (Huang et al., 1999). Very recently, Ouzzane and Aidoun (2003) proposed a one-dimensional model allowing to track flow conditions along the ejector. In their study, fluid properties were evaluated by using NIST (1980) subroutines for equations of state of refrigerants.

Despite their usefulness and the remarkable progress they provided for the general understanding of ejectors, this kind of studies were unable to correctly reproduce the flow physics locally along the ejector. It is the understanding of local interactions between shock waves and boundary layers, their influence on mixing and recompression rate, that will allow a more reliable and accurate design, in terms of geometry, refrigerant type and operation conditions. A way of achieving this objective at a reasonable cost is through CFD. Numerous CFD studies (Riffat et al., 1996; Chen et al., 1994;

Wang and Chen, 1996; Riffat and Everitt, 1999; Riffat and Omer, 2001; Desevaux and Aeschbacher, 2002; Desevaux et al., 2002) about supersonic ejectors have been achieved since the 1990s. However, some very fundamental problems have yet to be overcome, especially the modeling of shock-mixing layer interaction or ejector operation at different conditions. Indeed, some of them did not consider compressibility (Riffat et al., 1996) or turbulence (Chen et al., 1994; Wang and Chen, 1996). Moreover, even if some experimental comparisons were performed, they just dealt with global parameters and no local validations were achieved. Most of them used a relatively poor mesh resolution preventing any attempts to track shocks (Riffat et al., 1996; Riffat and Everitt, 1999; Riffat and Omer, 2001). In cases where turbulence was taken into account, no experimental validations or any justifications on the use of a particular model were carried out, except CPU cost. Very recently, Desevaux and Aeschbacher (2002) and Desevaux et al. (2002) obtained some local pressure measurements along the ejector with a capillary tube, and flow visualizations with laser tomography. The authors compared the results with their simulations by adjusting the pressure in the vacuum chamber or the secondary mass flow rate to reproduce ejector operation reasonably well. They concluded in this case that the standard *k*–epsilon model gave acceptable results compared to measurements.

As it is often the case in transonic compressible flows involving shock reflections and shock-mixing layer interaction, the choice of the turbulence model (Bartosiewicz et al., 2003) and grid refinements are crucial points. In addition, when measurements are performed, their influence should be evaluated or included in the model. Consequently, this paper aims at validating the choice of a turbulence model for the computation of supersonic ejectors in refrigeration applications. In order to limit the complexity of the model and to be able to use the available experimental data, air has been used as a working fluid. Six turbulence models, namely *k*–epsilon, realizable *k*–epsilon, RNG–*k*–epsilon, RSM and two *k*–omega have been tested and compared with measurements of Desevaux and Aeschbacher (2002) and Desevaux et al. (2002). The effect of the capillary tube has been also numerically evaluated. Later, the validated model has been used to qualitatively predict operation modes of a supersonic ejector, initially designed for refrigeration.

2. Modeling approach

2.1. Governing equations

The flow in the ejector is governed by the compressible steady-state axisymmetric form of the fluid flow conservation equations. For variable density flows, the Favre averaged Navier–Stokes equations are more suitable and will be used in this work. The total energy equation including viscous dissipation is also included and coupled to the set with the perfect gas law. The thermodynamics and transport properties for air are held constant; their influence was not found to be significant with the validation runs. The governing equations can therefore be written in their compact Cartesian form:

$$\frac{\partial \rho}{\partial t} + \frac{\partial}{\partial x_i}(\rho u_i) \tag{1}$$

$$\frac{\partial}{\partial t}(\rho u_i) + \frac{\partial}{\partial x_j}(\rho u_i u_j) = -\frac{\partial P}{\partial x_i} + \frac{\partial \tau_{ij}}{\partial x_j} \tag{2}$$

$$\frac{\partial}{\partial t}(\rho E) + \frac{\partial}{\partial x_i}(u_i(\rho E + P)) = \vec{\nabla} \cdot \left(\alpha_{\text{eff}} \frac{\partial T}{\partial x_i} + u_j(\tau_{ij}) \right) \tag{3}$$

$$\rho = \frac{P}{rT} \tag{4}$$

with

$$\tau_{ij} = \mu_{\text{eff}} \left(\frac{\partial u_i}{\partial x_j} + \frac{\partial u_j}{\partial x_i} \right) - \frac{2}{3} \mu_{\text{eff}} \frac{\partial u_k}{\partial x_k} \delta_{ij} \tag{5}$$

Although the steady state is desired, the unsteady term is conserved since from a numerical point of view, governing equations are solved with a time marching technique (see algorithm section).

2.2. Turbulence modeling

Most of the turbulence models used in this paper rely on the Boussinesq hypothesis. It means that they are based on an eddy viscosity assumption, which makes the Reynolds stress tensor coming from equation averaging, to be proportional to the mean deformation rate tensor:

$$-\rho \overline{u_i' u_j'} = \mu_t \left(\frac{\partial u_i}{\partial x_j} + \frac{\partial u_j}{\partial x_i} \right) - \frac{2}{3} \left(\rho k + \mu_t \frac{\delta u_i}{\delta x_i} \right) \delta_{ij} \tag{6}$$

The advantage of this approach is the relatively low computational cost associated with the determination of the turbulent viscosity. However, the main drawback of this hypothesis is the assumption that the turbulence is isotropic. The *k*–epsilon, RNG–*k*–epsilon and *k*–omega models are based on this hypothesis. Only the Reynolds stress model (RSM), tested in this study does not rely on this assumption, but the associated CPU cost may be relatively high. This latter, has been successfully used for supersonic jets and it is presented in Bartosiewicz et al. (2002). Based on our simulation results, RNG and *k*–omega–sst models appear to be very promising for ejector analysis. They are therefore described in more detail. The description of the other models listed can be found in Wilcox (1994).

2.2.1. The RNG-k–epsilon model (RNG)

The RNG model is derived from the exact Navier–Stokes equations, using a mathematical technique called "ReNormalization Group". The transport equation for epsilon differs from the standard model by new analytically determined constants and a new term:

$$\frac{\partial}{\partial x_i}(\rho\varepsilon u_i) = \frac{\partial}{\partial x_j}\left[\alpha_\varepsilon \mu_{\text{eff}} \frac{\partial \varepsilon}{\partial x_j}\right] + C_{1\varepsilon}\frac{\varepsilon}{k}G_k - C_{2\varepsilon}\rho\frac{\varepsilon^2}{k} - R_\varepsilon \tag{7}$$

with

$$\begin{aligned} R_\varepsilon &= \frac{C_\mu \rho \eta^3 (1-\eta/\eta_0)}{1+\beta\eta^3}\frac{\varepsilon^2}{k} \\ \eta &= Sk/\varepsilon \\ \eta_0 &= 4.38, \quad \beta = 0.012 \end{aligned} \tag{8}$$

where G_k, Y_M, and S are respectively the production of turbulence kinetic energy due to velocity gradients (Launder and Spalding, 1972), the contribution of dilatation–dissipation in compressible turbulence, and the modulus of the mean strain tensor. As a result, for weakly strained flow ($\eta \approx \eta_0$), this additional term has no contribution, and RNG tends to give comparable results than the k–epsilon model. But in regions of large strain rate ($\eta > \eta_0$), the R_ε term may have a significant contribution, which yields a lower turbulent viscosity than the standard k–epsilon model. In addition, the inverse effective Prandtl numbers α are computed using analytical formula derived by the RNG theory (Choudhury, 1993). In the same way, the model constants are also derived analytically: $C_{1\varepsilon} = 1.42$, $C_{2\varepsilon} = 1.68$. The eddy viscosity is computed using the classical relation with $C_\mu = 0.0845$:

$$\mu_t = \rho C_\mu \frac{k^2}{\varepsilon} \tag{9}$$

2.2.2. The standard and sst–k–omega models

This approach was first proposed by Wilcox (1988) and consists in replacing the equation for epsilon by a transport equation for $\omega = \varepsilon/k$. This equation, in the case of the standard formulation is

$$\frac{\partial}{\partial t}(\rho\omega) + \frac{\partial}{\partial x_i}(\rho\omega u_i) = \frac{\partial}{\partial x_j}\left[\left(\mu + \frac{\mu_t}{\sigma_\omega}\right)\frac{\partial \omega}{\partial x_j}\right] + G_\omega - Y_\omega \tag{10}$$

where G_ω and Y_ω are the production and the dissipation of omega respectively. The former has the same form than the k–epsilon model and is then also evaluated in a manner consistent with the Boussinesq hypothesis (Wilcox, 1988). The latter includes the compressibility effects and will be further explained. The turbulent viscosity is evaluated by combining k and ω:

$$\mu_t = \alpha^* \frac{\rho k}{\omega} \tag{11}$$

where the coefficient α^* is a function of the turbulence Reynolds number, and provides a damping of the turbulent viscosity in low Reynolds regions. In high Reynolds regions, $\alpha^* = 1$. This model works very well inside the boundary layer, but it has to be abandoned in the wake region and outside. The reason is that the standard k–omega model has a very strong sensitivity to the freestream conditions (Menter, 1992).

The shear stress transport (SST) version (Menter, 1994) of the k–omega model overcomes this deficiency because it is based on a blending approach. Indeed, to achieve the different desired features, the standard k–epsilon, turned into a k–omega formulation, is used from the wake region and outside; while the original model is used in the near wall region. To perform these features, a blending function F_1 is designed to be one inside the boundary layer and to change gradually to zero in the wake region. The resulting equation for ω is

$$\begin{aligned} \frac{\partial}{\partial t}(\rho\omega) + \frac{\partial}{\partial x_i}(\rho\omega u_i) = \frac{\partial}{\partial x_j}\left[\left(\mu + \frac{\mu_t}{\sigma_\omega}\right)\frac{\partial \omega}{\partial x_j}\right] + G_\omega - Y_\omega \\ + (1-F_1)D_\omega \end{aligned} \tag{12}$$

The term D_ω comes from the transformation of the k–epsilon model into a k–omega model (Menter, 1994). It can be view as an additional cross-diffusion term. Details on the expressions of F_1 and D_ω are provided in Menter (1994). In addition, the eddy viscosity is redefined so as to take into account the transport of the principal turbulent shear stress (Menter, 1994).

2.2.3. Wall functions

When appropriate, standards logarithmic wall functions are considered. Special care is given to the first cell location, by a local adaptation following y^+, such as $y^+ \leqslant 30$. If $y^+ < 11$, the classical linear law is taken for the sublayer. This treatment is consistent with the use of standard wall functions.

2.3. Algorithm

The governing equations are solved using the commercial CFD package FLUENT. In this respect, they are discretized using a control volume technique. For all equations, convective terms are discretized using a second-order upwind scheme: inviscid fluxes are derived using a second order flux splitting (Roe, 1981, 1986), achieving the necessary upwinding and dissipation close to shocks. The interface flux is determined by separate terms, which depends on the upstream and downstream sides of the face, so that the information passed through the face contains the flow characteristics. Diffusion terms are always cast into a central difference form. The resulting system is time-preconditioned, in order to overcome the numerical stiffness encountered at low Mach number. The discretized system is solved in

a coupled way with a Block Gauss Seidel algorithm. The time marching procedure uses a first-order implicit Euler scheme. In a second step, other scalar equations such as turbulence are solved in a segregated fashion.

2.4. Numerical accuracy and convergence

The criterion for assessing convergence was based on the root mean square of the density residues expressed by:

$$R(\varsigma) = \left[\sum_{i=1}^{N}\left(\frac{\partial \varsigma}{\partial t}\right)_i^2\right]^{1/2} \tag{13}$$

where N is the number of grid points and ς is the variable considered to check (mass, energy, momentum, etc.), e.g. the mass conservation is based on the density residues. Generally, computations are stopped when residues fall below 1×10^{-6} and when the solution was no longer changing.

In addition, at convergence, the mass imbalance is checked on each inlet and outlet boundaries:

$$\left|\frac{\sum m_{\text{in}} - \sum m_{\text{out}}}{\sum m_{\text{in}}}\right| \leqslant 1 \times 10^{-5} \tag{14}$$

Because a time marching solver is used, the required time step is set owing to a Courant–Friedrichs–Lewy (CFL) condition that ensures the acoustic waves and flow physics are properly tracked by the solver. During first iterations the CFL is set to 0.5 because changes in the solution are highly non-linear, and it is adjusted along iterations as the solution progresses. Its maximum value may be larger than 1 due to the implicit nature of the time discretization. In addition, an adaptative unstructured mesh is used to better track shock waves and gradients. For each case, a grid convergence study is performed to get minor differences between the final and the previous adaptation step, typically less than 5.

3. Experimental setup

3.1. Flow facility

The experimental installation is schematized in Fig. 2. A screw compressor of sufficient capacity is used to ensure the continuous operation of the ejector. Compressed air (at a maximum pressure of 8 bar) is filtered to remove large particles such as dust, and compressor oil droplets. The compressed air is then directed towards an air reservoir, which is connected to the entrance of the primary nozzle of the ejector just after passing through a pressure control valve to adjust the primary stagnation pressure P_1. The induced fluid is air taken from the surrounding atmosphere. The induced mass flow rate m_2 can be regulated by means of a valve located at the entrance of the aspiration duct. Apparatus installed on the primary and secondary air circuits for measurement of stagnation pressures and flow rates is also shown in Fig. 2.

3.2. Centerline pressure measurement system

Static pressure measurements along the ejector centerline were performed by means of a sliding measuring system (Desevaux et al., 1994). The probe, as shown in Fig. 3, consists of a capillary tube (external diameter of 1 mm, internal diameter of 0.66 mm) located on the ejector axis. Static pressure is measured through a hole of 0.3 mm diameter, which crosses the tube radially, and the value is then transmitted to an absolute pressure transducer. The translation of the tube provides static pressure measurements along the pseudo-shock region (between the inlet section of the primary nozzle to the exit section of the diffuser.

Measurements were taken for three different pressures at the primary inlet: 4 atm, 5 atm, and 6 atm respectively. Concerning the comparison with the numerical

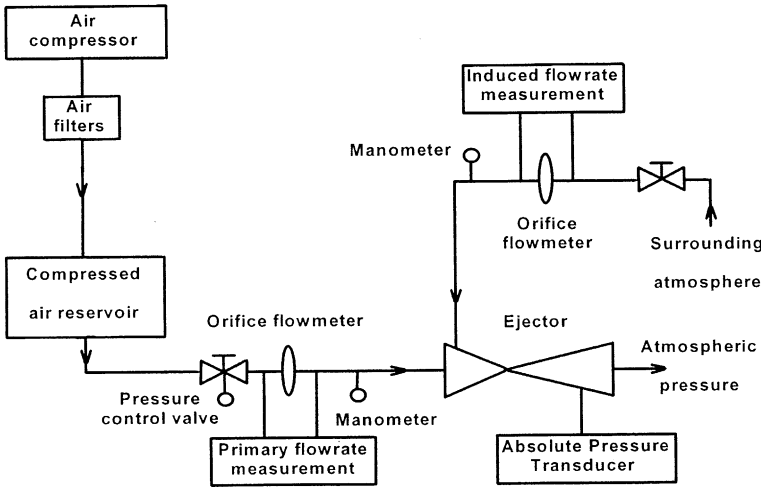

Fig. 2. Experimental apparatus.

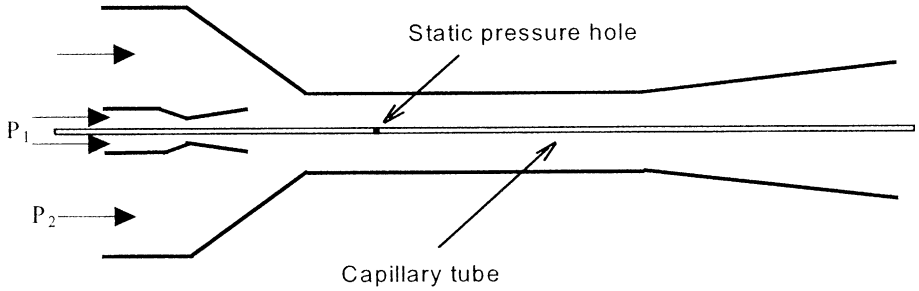

Fig. 3. Capillary probe to measure the centerline pressure.

results presented in this paper, some tests were performed with no induced flow but with the probe insertion; and some with an induced flow without the probe insertion, for each pressure cited above.

4. Validation

4.1. Flow physics and boundary conditions

The ejector geometry with its characteristics dimension is depicted Fig. 1. At some appropriate level of the exit pressure (P_3), the primary stream (1) is accelerated through a convergent–divergent nozzle to a supersonic velocity. The secondary stream (2) is then drawn by an entrainment effect. Depending on the geometrical design, the resulting stream may reach sonic speed again inside the constant area duct. Along this duct, the flow follows a succession of normal and/or oblique shock waves, also called a shock train region (Fig. 4), and involving a pressure rise (Matsuo et al., 1999). Farther downstream, the pressure inside the motive stream is adjusted with that of the secondary stream to attenuate the shocks until they disappear. Following this zone, the primary stream may be still supersonic as observed by Bartosiewicz et al. (2002). In addition, it is noted that the pressure still increases until a maximum value is reached. This fact is consistent with one-dimensional theory for a supersonic flow inside an adiabatic duct with friction. The region of the total pressure rise, from the outlet of the primary nozzle, is referred as "pseudo-shock" (Matsuo et al., 1999). Downstream of this point, the motive jet becomes subsonic and friction makes the pressure decrease. Depending on this pressure recovery, the flow should have sufficient energy in terms of total pressure to reach the final pressure (P_3) at the diffuser. Further details on the different flow regions can be found in Matsuo et al. (1999).

At inlets (labels 1 and 2 in Fig. 1), total pressures, total temperatures, and flow direction consistent with flow characteristics (subsonic) are prescribed. At exit (label 3), the pressure is fixed when the flow is subsonic, and

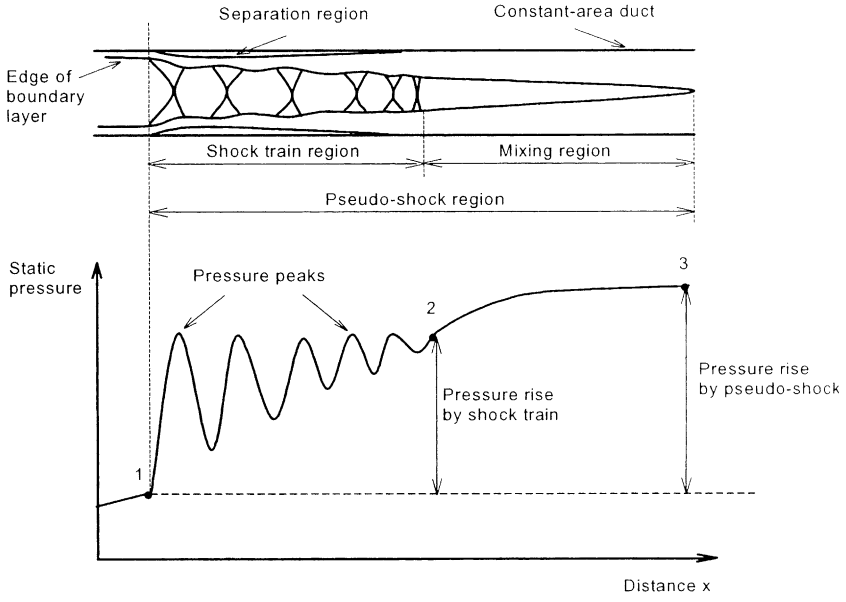

Fig. 4. Description of the different flow regions.

extrapolated from interior when the flow is supersonic. In refrigeration, this pressure is that of the condenser, while P_1 is the generator pressure and P_2 is the evaporator pressure. In this study all the walls are considered to be adiabatic with no slip. For turbulence, it is considered that inlet flows have a turbulence intensity of 5% that matches with the value in a fully developed pipe.

4.2. Results: operation with no secondary flow

For these tests, there is no secondary inlet. The motive total pressure is successively set to 4, 5, 6 atm, and the total temperature is kept constant at 300 K. In order to validate the choice of the turbulence model, the case for $P_1 = 5$ atm is taken as a reference. The selected model will then be applied for other operating pressures. In all cases, the exit pressure is kept constant equal to $P_3 = 1$ atm.

Fig. 5 illustrates the results for the axial pressure based on different turbulence models, plotted from the primary nozzle outlet. It is clear that neither k–epsilon based models (k–epsilon, R-k–epsilon or RNG) nor RSM model are able to represent correctly the shock reflection pattern. Numerical results almost show phase opposition for the shock reflections. However, the qualitative evolution of pressure recovery is well represented. At $X = 0.14$ m the maximum difference in comparison with measurements is about 6%. In addition, a difference of 20% is observed at the outlet of the primary nozzle. For this case, the one-dimensional theory gives a ratio $P/P_1 = 0.075$ at the nozzle exit. The discrepancy between this value and the predicted numerical value is approximately 6.5%. The difference may be due to condensation that has been observed experimentally.

In the following computations, a capillary probe is accounted for the numerical model. This has been implemented by including a solid core around the axis. The probe diameter is 1 mm, and coupled heat transfer conditions are applied on it. The probe changes the flow topology, making the shock reflections become annular. Fig. 6 shows the adapted mesh around the probe, where it is possible to guess the location of incident and reflected waves.

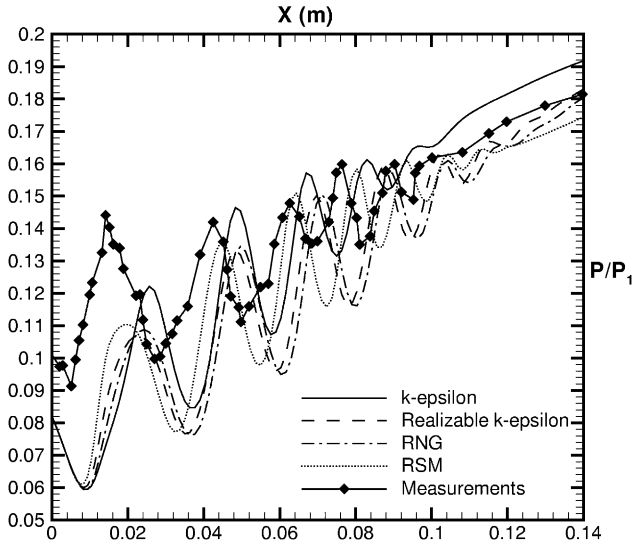

Fig. 5. Axial pressure vs measurements or several turbulence models.

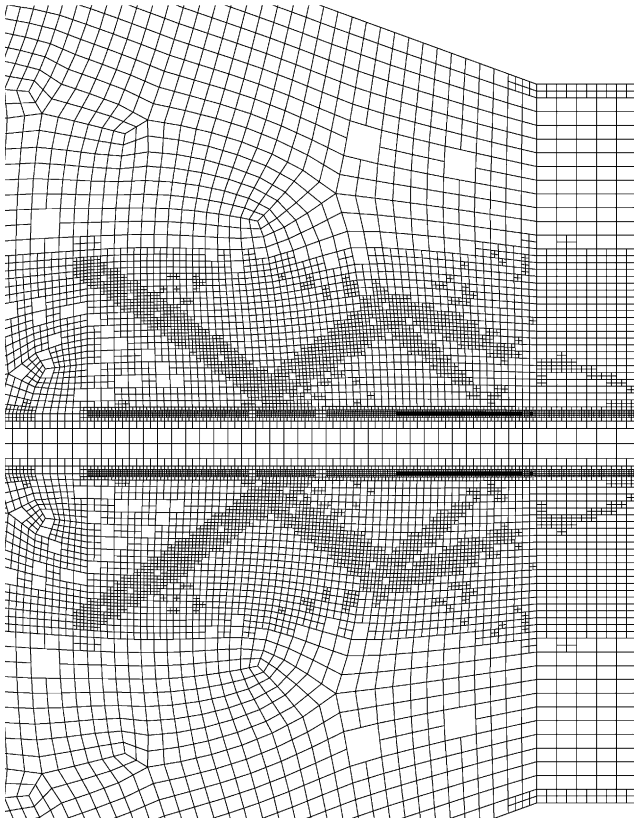

Fig. 6. Adapted mesh around shocks and near the probe surface.

Fig. 7 presents the effect of the probe on the axial pressure profiles in the case of the k–epsilon model (Fig. 7a) and the RNG model (Fig. 7b). In both cases, the correlation with measurements has significantly improved, showing the probe has a noticeable effect on the flow even if it is relatively small. Indeed the area ratio between the probe and the mixing duct is about 1.7×10^{-2}.

For the RNG model, the improvement is even better, because the reflections phase is in excellent agreement with measurements (Fig. 7b). The effect of adaptation is also demonstrated where sharper shock can be observed. In addition, it is observed that errors are more important in expansions than in compressions. For the former the difference is about 10%, while for the latter it is 35–50%. Once again, the presence of condensation in the flow may inhibit compressibility effects by smoothing out the shock and expansion waves. However, further investigations are thought to be necessary and will be performed in order to check this hypothesis. Never-

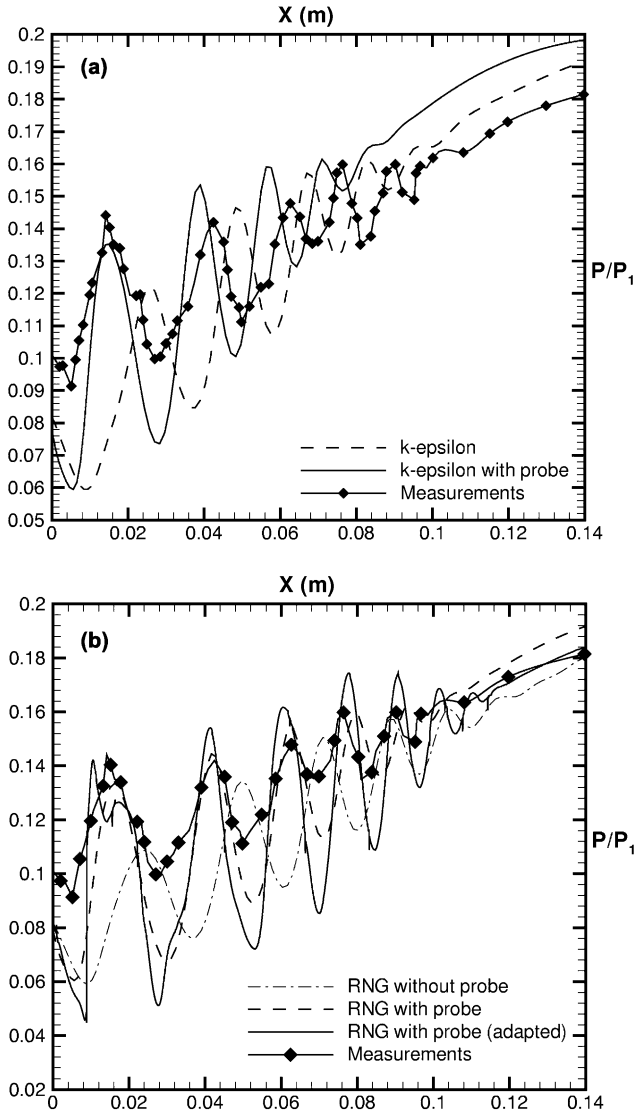

Fig. 7. Effect of the probe on computational results.

theless, shock locations and the average pressure recovery seem to be correctly represented by the RNG model.

For all the other turbulence models, the modeling of the pressure probe provided clear improvement over the computations without the probe insertion, but their performance was lower than that of the RNG.

Fig. 8 compares the performance of the two *k*–omega models with that of the RNG. The standard *k*–omega model over-predicts shock amplitude, and fails in predicting shock location after the fourth peak. This confirms observations of Menter (1992) on the use of *k*–omega model outside boundary layers. The *k*–omega–sst model gives comparable results to those of RNG, but it tends to under-predict the average line of pressure recovery after the fifth compression. Farther downstream (not shown), both models give the same pressure. However additional tests are required to check which model performs better for ejector modeling.

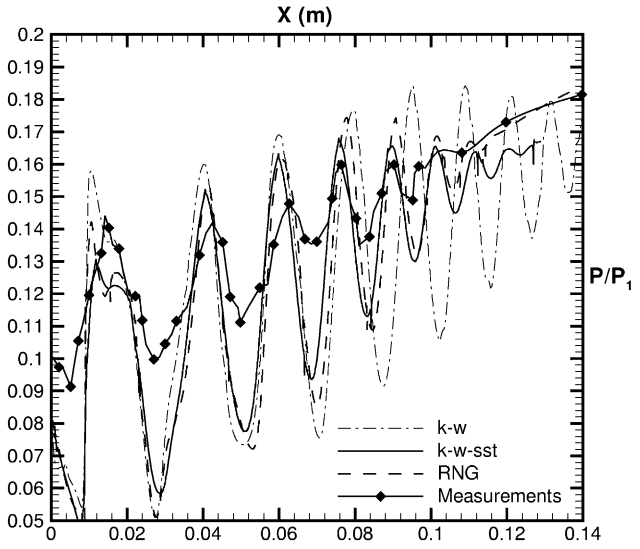

Fig. 8. Comparison between the RNG and the two *k*–omega models.

Two other motive pressures have been tested for these two turbulence models. Fig. 9 shows results for $P_1 = 4$ atm (a) and $P_1 = 6$ atm (b). For $P_1 = 4$ atm, the jet issuing from the primary nozzle is strongly overexpanded, the first compression is strong. For $P_1 = 6$ atm, it becomes underexpanded and the flow firstly proceeds to an expansion. The first compression is smoothed because it occurs in the more confined mixing duct. For $P_1 = 4$ atm, shock locations are in very good agreement with experimental data. The same discrepancy is observed for expansion amplitudes. Measurements are still a little more dissipative compared to numerical results. However, pressure recovery is very well predicted, although the sst–*k*–omega model tends to under-predict the average line of pressure before eventually reaching the same value (Fig. 9a).

For $P_1 = 6$ atm (Fig. 9b), shock locations are also well represented, even though the dissipation effect of measurements is more pronounced downstream of $X = 0.1$ m. The two first shocks are under-predicted, and the model fails to predict the location of the second shock as accurately as for the remaining shocks. In addition the total pressure available at $X = 0.14$ m is larger for the strongly overexpanded case of $P_1 = 4$ atm, positively impacting on ejector operation in case of refrigeration applications. However, additional studies are needed to investigate about optimal ejector operation and design.

4.3. Preliminary validation for an induced flow ejector

In this part, the secondary mass flow rate is experimentally kept constant ($m_2 = 0.028$ kg/s) by means of a control valve. In the model, the mass flow rate is also fixed, the secondary pressure being computed to match this flow rate is compared with experimental data. In these tests, the capillary pressure probe is removed from

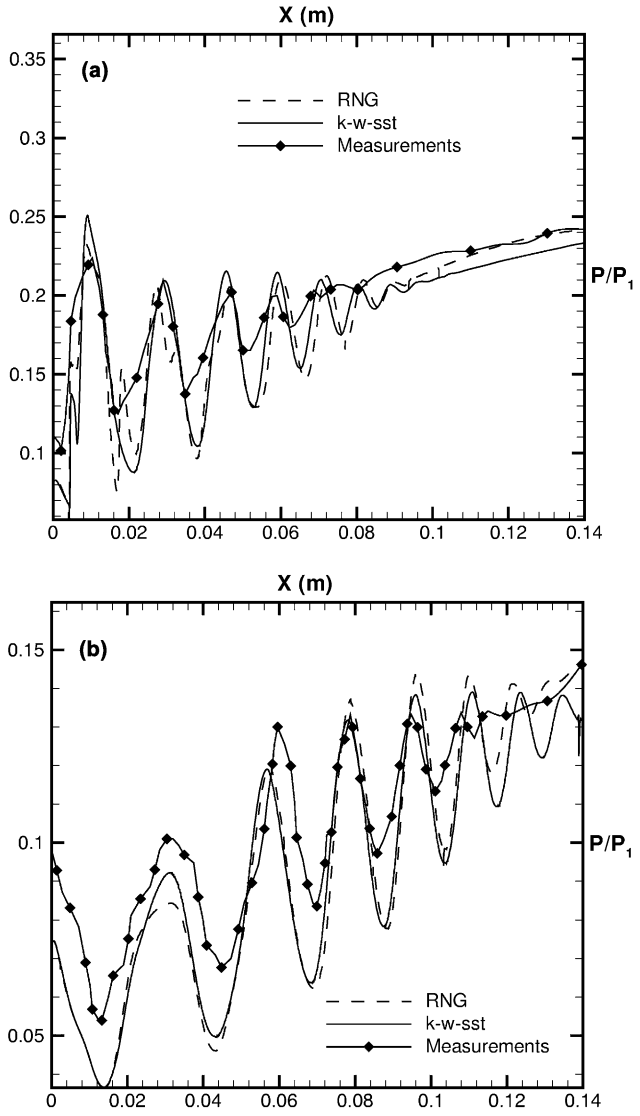

Fig. 9. Centerline pressure for $P_1 = 4$ atm and $P_1 = 6$ atm.

the ejector, and a laser tomography facility is used to visualize the flow in the mixing duct. Details of this technique can be found in Desevaux and Aeschbacher (2002) and Desevaux et al. (2002). From these visualizations, it is possible to establish the non-mixing length between the core and the secondary flows: The core of the flow is darker than the fringes and the outer flow. As a numerical tracer, a passive scalar is used for comparison with the laser tomography pictures. For a scalar Γ the steady state transport equation can be written:

$$\frac{\partial \rho_\Gamma u_i \Gamma}{\partial x_i} = \frac{\partial}{\partial x_i}\left(\mu_\Gamma \frac{\partial \Gamma}{\partial x_i}\right) \tag{15}$$

where $\rho_\Gamma = \rho$ and $\mu_\Gamma = \mu_l + \mu_t = \mu_{\text{eff}}$. This tool gives qualitative information about the mixing regions (length of non-mixing), and even about the quality (under certain conditions) of mixing by checking Γ values. At the primary inlet $\Gamma = 0$ is fixed, while $\Gamma = 1$ is prescribed at the secondary inlet. Finally, walls are considered non-permeable to this numerical colorant.

Table 1
Non-mixing length and secondary pressure

P_1 (atm)	4	5	6
P_2 (measured) (atm)	0.78	0.68	0.4
P_2 (computed) (atm)	0.61	0.52	0.4
l_m (measured) (m)	0.13	0.17	0.21
Measurement error (+/− %)	15	12	9.5
l_m (computed) (m) RNG	0.16	0.18	0.21
l_m (computed) (m) k–omega–sst	0.14	0.17	0.21
Error/measurements (%) (RNG)	23	6	0
Error/measurements (%) (k–omega–sst)	8	0	

Table 1 illustrates results for the computed secondary pressure P_2 and for the non-mixing length. The non-mixing length is numerically evaluated by the location at which Γ starts to increase from zero. Both models give comparable results concerning the secondary pressure P_2. It is shown that for $P_1 = 6$ atm the agreement with experimental data is excellent for both the secondary pressure and the non-mixing length. For $P_1 = 5$ and $P_1 = 4$ atm the models under-predict P_2 of 23% and 24% respectively. It is also shown that the k–omega–sst gives better performance for the prediction of the non-mixing length. This parameter is very important in the design of ejectors in refrigeration.

5. Modeling ejector operation

In this part, the ejector dimensions have been modified in accordance with Ouzzane and Aidoun (2003). In this case, the ejector was essentially designed for refrigeration applications even though air is taken as the working fluid in the present paper. The following sections will be focussed on the modeling of ejector operation over a wide range of operating conditions. At this point, it may be needed to define the terms "on-design" and "off-design". For fixed geometry and compression ratio (P_3/P_1), the on-design point is defined by the conditions giving the maximum entrainment ratio for this pressure, e.g. the critical point in Fig. 10. If the maximum entrainment ratio is desired whatever the backpressure, the on-design region is given by $P_3 \leqslant P_3^*$ (Fig. 10). Both cases require that not only the primary nozzle is chocked, but also the secondary, which means the secondary stream must reach sonic condition. However, in a real case, P_3 is generally fixed by the system or by the operating conditions prevailing downstream (condenser pressure in refrigeration applications). The purpose is then to find operating conditions (for the primary stream) and the geometrical design providing a maximum secondary mass flow rate for a given P_2.

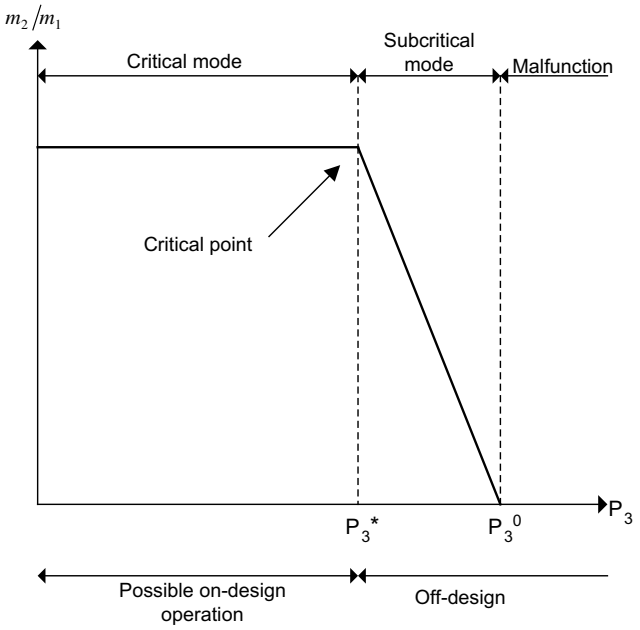

Fig. 10. The different modes of operation for a supersonic ejector.

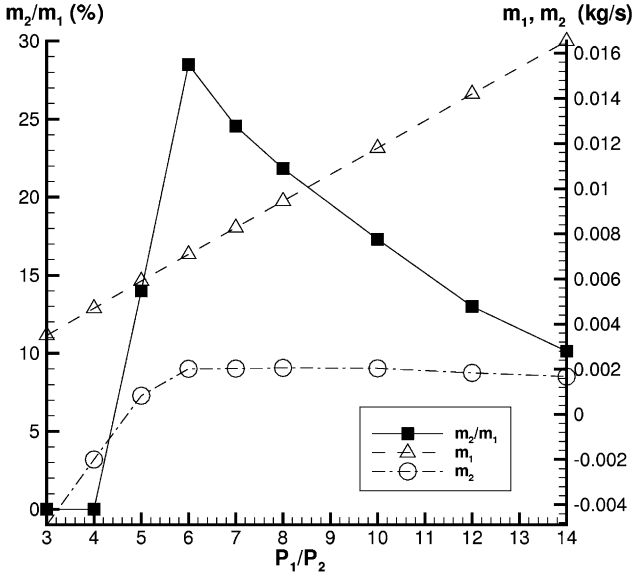

Fig. 11. Entrainment ratio and ejector chocking.

For cases where the secondary flow is not choked, the secondary mass flow rate and the backpressure P_3 are closely coupled in such a way that the ejector performance is strongly sensitive to these parameters. This case is called the off-design mode (Fig. 10) where a slight change in the backpressure may involve a strong decrease of the entrainment ratio. In some cases, if P_3 is too high compared to the total pressure of the flow, severe backflows may occur and the ejector does not work properly (ejection of flow at the secondary inlet and/or backflow at outlet).

5.1. Modeling the different modes of operation

This section assesses the ability of CFD to represent the different modes of supersonic ejector operation, from the malfunctioning to the on-design mode. In this respect, the pressures downstream and at the secondary inlet were fixed in order to guarantee the desired compression rate:

$$P_3 = 1 \text{ atm}$$
$$P_2 = 0.5 \text{ atm} \qquad (16)$$
$$\frac{P_3}{P_2} = 2$$

The motive pressure (P_1) is then changed so as to sweep a wide range of operating conditions. For each case, the secondary mass flow rate is computed. The results for the nine tested ratios of (P_1/P_2) are plotted in Fig. 11.

For $P_1/P_2 = 3$ and $P_1/P_2 = 4$, the ejector does not work properly: some fluid is rejected from the secondary inlet instead of being drawn. In the first case, a straight shock occurs in the primary nozzle. The flow downstream becomes sonic and the information on the backpressure is transmitted through the entire flow. As a result of an adverse pressure gradient at the secondary inlet, an outflow is then provoked. For the second case, the primary nozzle is fully supersonic, but conditions at its outlet are highly overexpanded, resulting in a strong shock or a Mach disk right downstream of the nozzle exit, in the supersonic jet. The flow becomes again wholly subsonic, and the kinetic energy exchange with the secondary stream is not sufficient. This condition also results in a backflow with a very high total pressure loss across the shock.

For the other ratios, it is observed that the primary mass flow rate m_1 varies linearly with P_1 (or P_1/P_2), in full agreement with the one-dimensional theory. Moreover, the ejector starts to draw some fluid from the secondary inlet for a value of the ratio P_1/P_2 between 4 and 5 (Fig. 11). As the primary pressure increases, the secondary mass flow rate increases too, but remains very sensitive up to $P_1/P_2 = 6$ (Fig. 11): this is the off-design mode. The choking of the ejector occurs for $6 < P_1/P_2 < 7$ where the on-design point is reached (Fig. 11, maximum m_2/m_1). However, more tests will be necessary to precisely determine the on-design value between these two pressures. Beyond this point, the secondary mass flow rate remains almost constant and less sensitive to P_1 (Fig. 11).

Nevertheless, it is observed that the secondary mass flow rate may change once the entrained stream is choked (Fig. 11), and these changes may be quite significant: the difference for the induced mass flow rate (m_2) between $P_1/P_2 = 8$ and $P_1/P_2 = 12$ is 10.7%; between

$P_1/P_2 = 8$ and $P_1/P_2 = 14$ it is 18.6%. This fact is of primary importance because the entrainment is driven by two effects: on one hand the flow is drawn due the low pressure induced by the primary stream and it crosses an equivalent critical section between the outer wall and the core flow. On the other hand the mass of secondary fluid drawn into the ejector also depends on the shear stress, and therefore on the contact surface, between both streams. For the cases $P_1/P_2 = 7$ and $P_1/P_2 = 8$, the supersonic jet at the nozzle exit is very slightly overexpanded, because streamlines tend to slightly converge toward the jet center as can be seen on the isoMach $M = 1$ (Fig. 12). For these cases, the ejector becomes choked near the middle or in the second half of the constant area duct. For higher pressure ratios (for $P_1/P_2 = 10$, 12, 14), the jets become more and more underexpanded, and therefore the flow tends to diverge right from the nozzle exit. This divergence involves a smaller cross-section for the secondary flow, giving rise to good conditions for choking phenomenon. In these conditions, the sonic line reaches the wall region more upstream than for the previous pressures ($P_1/P_2 = 7$, 8) and the ejector is then choked close to the entrance of the mixing duct (Fig. 12). For these later cases, one may assume that the shear stress effect is less efficient than the pressure and critical section effect because the contact surface between both fluids is shorter as the secondary stream becomes choked over a small distance. Further tests will however be required to quantify the magnitude of these two effects on the entrainment ratio.

Finally, it is observed that the maximum m_2 does not match with the on-design point (m_2/m_1 maximum): $P_1/P_2 = 6$, $m_2 = 0.00202$ kg/s and for $P_1/P_2 = 8$, $m_2 = 0.00206$ kg/s. Actually the additional amount of energy required to compress the primary stream from $P_1/P_2 = 6$ to $P_1/P_2 = 8$ is very important in comparison to the gain made in terms of secondary mass flow rate.

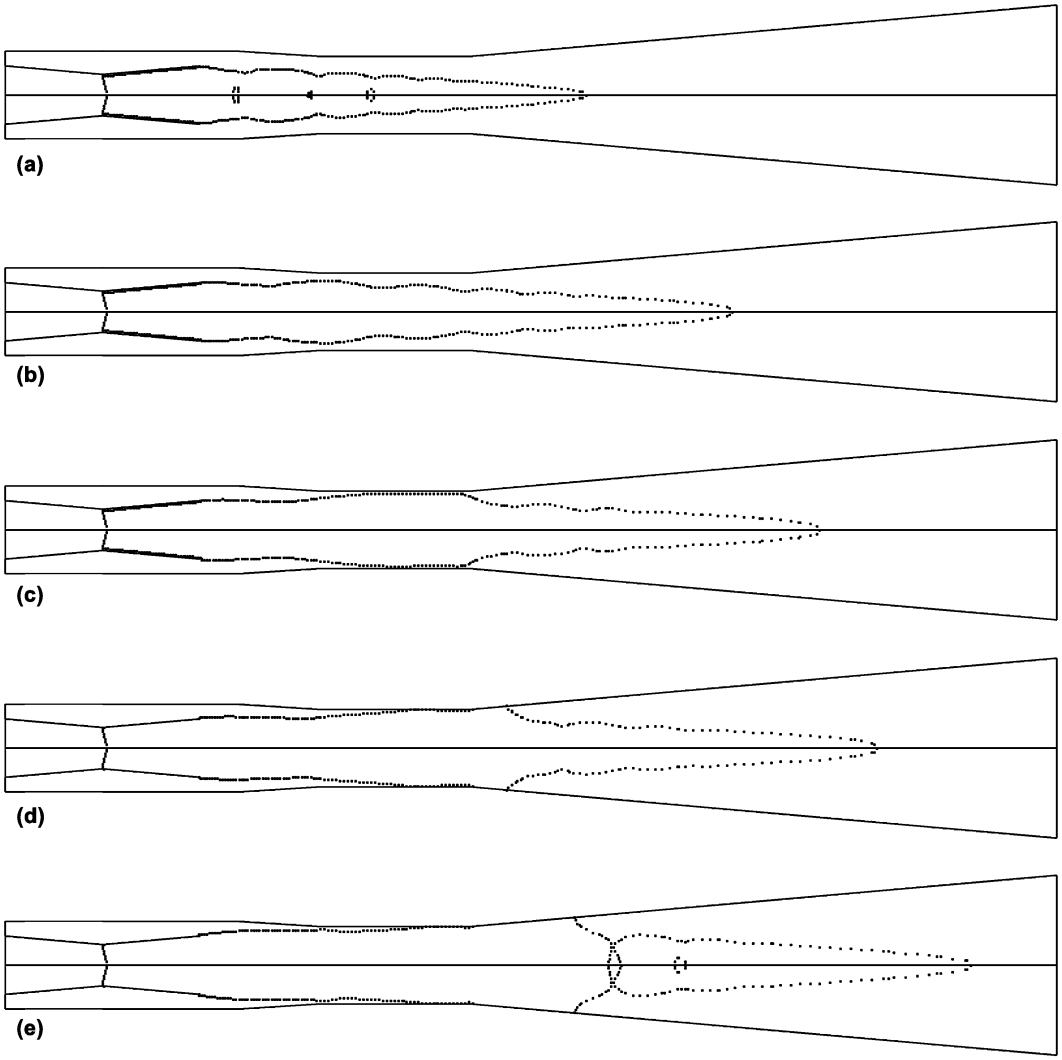

Fig. 12. Sonic line (isoMach $M = 1$) for (a) $P_1/P_2 = 5$, (b) $P_1/P_2 = 6$, (c) $P_1/P_2 = 7$, (d) $P_1/P_2 = 8$ and (e) $P_1/P_2 = 10$.

5.2. CFD as a diagnosis tool for the operation of supersonic ejectors

In the previous section, CFD was used to model ejector operation, analyse the different phenomena during the process and assess performance. In this section, it is shown how CFD can help to identify the cause of a poor performance and to evaluate the quality of the mixing, which is a key operation parameter.

As previously described, the performance of a supersonic ejector in terms of entrainment is based of an energy exchange between motive and secondary streams.

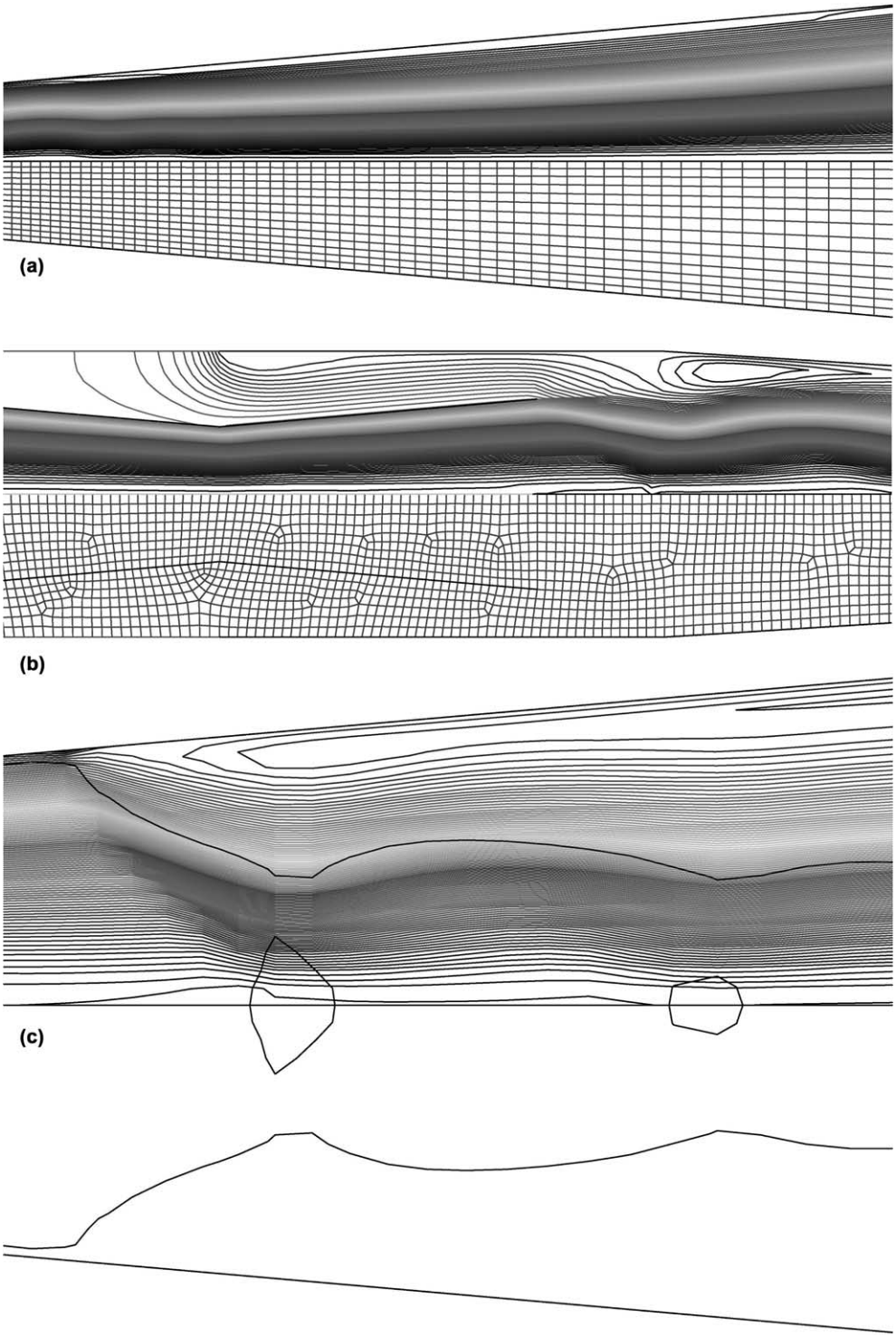

Fig. 13. Shock induced boundary layer separation: (a) $P_1/P_2 = 6$ (diffuser), (b) $P_1/P_2 = 5$ (primary nozzle) and (c) $P_1/P_2 = 12$ (diffuser).

Fig. 12a shows that for $P_1/P_2 = 5$, the motive jet exhibits strong shocks or Mach disk up to the third shock cell. This represents a high irreversible energy loss that the primary flow will not be able to exchange with the secondary stream. Indeed such strong shocks may result in a boundary layer separation. Fig. 13b illustrates how a Mach disk in the supersonic motive jet may induce separation of the secondary flow near the primary nozzle exit. This kind of relatively strong recirculation may harm the secondary stream entrainment, which may explain why such a difference exists in terms of entrainment ratio in comparison with $P_1/P_2 = 6$. Fig. 13a shows that the occurrence of shocks in the diffuser results in a slight boundary layer separation. However, this separation is not critical and the boundary layer reattaches farther downstream (Fig. 13a). On the contrary, for the case $P_1/P_2 = 12$, the flow Mach number is too high at the diffuser entrance, giving rise to the occurrence of two strong shocks (Fig. 13c). At this level of Mach number, the shock-boundary layer interaction is important (Matsuo et al., 1999) giving rise to a bifurcated shock shown in Fig. 13c. This figure shows the flow streamlines with the sonic-line highlighted. The first Mach disk is the strongest, involving a strong boundary layer separation. The sonic-line illustrates the bifurcation point that gives rise to the flow separation (Fig. 13c). This transition toward a bifurcated shock begins at $P_1/P_2 = 10$. Phenomena such as this have negative consequences on ejector operation, because they limit the entrainment ratio, and some outer fluid possibly coming from the condenser in refrigeration applications, can be drawn.

An other convenient tool provided by the CFD, which may be used to evaluate stream mixing, is the transport and diffusion of a passive scalar. When its properties are chosen such that its inertia and diffusion

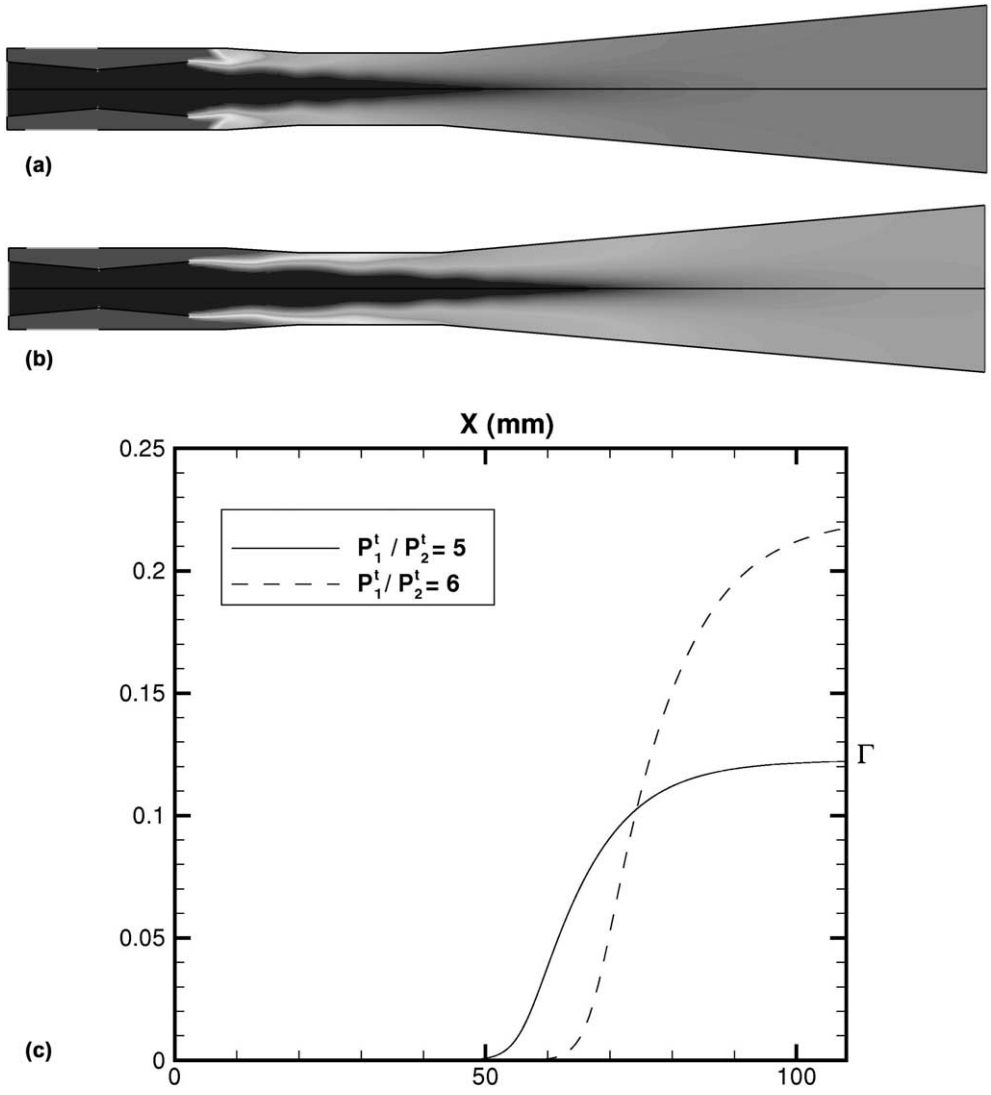

Fig. 14. Contour ((a) $P_1/P_2 = 5$, (b) $P_1/P_2 = 6$) and axial profile of the numerical colorant.

be zero for the local flow (Eq. (15)), it can be used as a perfect marker or numerical colorant. Fig. 14 shows results for a numerical colorant injected into the secondary flow, in order to characterize mixing for $P_1/P_2 = 5$ and $P_1/P_2 = 6$ cases. The contour plot for $P_1/P_2 = 5$ shows the effect of recirculation immediately downstream of the primary nozzle, limiting the secondary flow rate (Fig. 14a). In addition, the results illustrate that the mixing duct is too short to achieve proper mixing between both streams (Fig. 14c). Indeed, complete mixing begins at the end of this section or even in the diffuser whose inlet is located at $X = 48$ mm. In ideal conditions, mixing should be completed at the end of the constant area duct, in order to take advantage of the maximum pressure recovery (Matsuo et al., 1999) before the flow enters the diffuser. Moreover, it clearly appears that the quality of the mixing process is better for $P_1/P_2 = 6$ when the asymptotic values of Γ are high (Fig. 14c): This parameter appears to be directly related to the entrainment ratio. For the other P_1/P_2 ratio, it has been verified that the maximum Γ values were below that for $P_1/P_2 = 6$. Consequently the parameter Γ can be used as stream mixing indicator, which may be used for the ejector mixing chamber design.

6. Conclusion

The first part of this paper was concentrated on the validation of a CFD tool for simulation, analysis and design of supersonic ejectors in refrigeration applications. The validation was primarily focussed on the choice of the more suitable turbulence model in terms of correct representation of physical phenomena, acceptable accuracy in the quantitative predictions for design purposes (entrainment, mixing) and computational cost. It has been shown that the RNG and k–omega–sst models were the best suited to predict the shock phase, strength, and the mean line of pressure recovery. However, the k–omega–sst model has further shown better performances in term of stream mixing. The most important drawbacks for any model is related to its ability to correctly predict the strength of the expansion cells. Further investigations have to be performed in order to assess the importance of condensation on the amplitude of expansion-shock cells and find out whether a multiphase model should be considered.

In addition, the CFD-experiment integration approach allowed to evaluate the interaction between the capillary probe and the flow, despite the fact that much care was taken to minimize flow disturbance. In order to study the mixing in an ejector operating with a secondary flow, a numerical colorant has been used. The results were compared with those of laser tomography pictures. The secondary pressure has been accounted for in the comparisons. For the highest pressure, numerical results were in excellent agreement with experimental data. But, as the primary pressure was decreased, some discrepancy between simulation and measurements was observed for the secondary pressure. There is no satisfactory explanation at this point for this departure from experimental data. However, there are some aspects that cannot be modeled such as pressure losses induced by the upstream fluid flow and the control valve (at the secondary inlet). In addition, the tracers consisting of water particles due to condensation or oil droplets, and used to evaluate the non-mixing length are probably non-ideal; their diffusion coefficient may perhaps be a function of local conditions.

The second part was devoted to the use of the validated model in order to study from a qualitative point of view, different modes of operation of a supersonic ejector. This study was mainly focused on a supersonic ejector functioning as static compressor for refrigeration applications. In this case, CFD proved its ability to model different operation modes ranging from on-design operation, with maximum capacity (choking), to complete malfunctioning (flow rejection at the secondary inlet, flow drawn at the outlet). Moreover, CFD has been used to diagnose the performance (mixing quality) or faulty operation (shock-induced flow separation). Coupled with experimental tests, this feature can help to efficiently improve ejector design.

Although extensive validation has been performed in order to select a turbulence model capable of capturing local features such as shocks locations and the non-mixing length, validation tests are still required over a wide range of operating conditions for the global operation. A modification of the experimental setup is prepared for this purpose to conduct new tests and investigate the condensation problem (experimentally and numerically). In addition, a refrigeration-oriented model is under development.

Acknowledgments

Financial support for this work was partly provided by the Canadian Federal Government's Program on Energy Research Development (PERD) and by the Innovative Research program (IRI).

References

Aidoun, Z., Ouzzane, M., in press. The impact of ejector characteristics on the operation and performance of a conventional refrigeration cycle. Conference Proceedings, ISHTEE 2003, Guangzhou, China, 12–15 January 2004.

Alperin, M., Wu, J.-J., 1983a. Thrust augmenting ejector, Part I. AIAA J. 21 (10), 1428–1436.

Alperin, M., Wu, J-J., 1983b. Thrust augmenting ejector, Part II. AIAA J. 21 (12), 1428–1698.

Bartosiewicz, Y., Mercadier, Y., Proulx, P., 2002. Numerical investigations on dynamics and heat transfer in a turbulent underexpanded jet. AIAA J. 40 (11), 2257–2265.

Bartosiewicz, Y., Aidoun, Z., Desevaux, P., and Mercadier, Y., 2003. CFD-experiments integration in the evaluation of six turbulence models for supersonic ejectors modeling. Conference Proc., Integrating CFD and Experiments, Glasgow, UK.

Chen, F., Liu, C.F., Yang, J.Y., 1994. Supersonic flow in the second-throat ejector–diffuser system. J. Spacecraft Rocket 31 (1), 123–129.

Choudhury, D., 1993. Introduction to the renormalization group method and turbulence modeling. Tech. Rep. TM-107, Fluent Inc., Lebanon, USA.

Desevaux, P., Aeschbacher, O., 2002. Numerical and experimental flow visualization of the mixing process inside an induced air ejector. Int. J. Turbo Jet Engines 19, 71–78.

Desevaux, P., Prenel, J.P., Jacquet, P., 1994. Static pressure measurement along the centerline of an induced flow ejector. Exp. Fluids 16, 289–291.

Desevaux, P., Lanzetta, F., Bailly, Y., 2002. CFD modelling of shock train inside a supersonic ejector: validation against flow visualization and pressure measurements in the case of zero-secondary flow. Conference Proc., 10th Int. Symp. on Flow Visualization, Kyoto, Japan.

Huang, B.J., Chang, J.M., Wang, C.P., Petrenko, V.A., 1999. A 1-D Analysis of ejector performance. Int. J. Refrigeration 22, 354–364.

Keenan, J.H., Newman, E.P., 1946. A simple air ejector. J. Appl. Mech. Trans. ASME 64, A75–A81.

Keenan, J.H., Newman, E.P, Lustwerk, F., 1950. An investigation of ejector design by analysis and experiments. J. Appl. Mech. Trans. ASME 72, 299–309.

Launder, B., Spalding, D., 1972. Lectures in Mathematical Models of Turbulence. Academic Press, London, England.

Matsuo, K., Miyazato, Y., Kim, H.-D., 1999. Shock train and pseudo-shock phenomena in internal gas flows. Progr. Aerospaces 35, 33–100.

Menter, F.R., 1992. Influence of freestream values on k-omega turbulence model predictions. AIAA J. 30 (6), 1651–1659.

Menter, F.R., 1994. Two-equations Eddy-viscosity turbulence models for enginnering applications. AIAA J. 32 (8), 1598–1605.

Munday, J.T., Bagster, D.F., 1977. A new ejector therory applied to steam jet refrigeration. Ind. Eng. Chem. Process Res. Dev. 16 (4), 442–449.

NIST Standard Reference Database 23 1980. NIST Thermodynamics and Transport Properties of Refrigerants and Refrigerant Mixtures, REFPROP, Version 6.01.

Ouzzane, M., Aidoun, Z., 2003. Model development and numerical procedure for detailed ejector analysis and design. Appl. Thermal Eng. 23, 2337–2351.

Riffat, S.B., Gan, G., Smith, S., 1996. Computational fluid dynamics applied to ejector heat pumps. Appl. Thermal Eng. 16 (4), 291–297.

Riffat, S.B., Everitt, P., 1999. Experimental and CFD modelling of an ejector system for vehicle air conditioning. J. Inst. Energy 72, 41–47.

Riffat, S.B., Omer, S.A., 2001. CFD Modelling and experimental investigation of en ejector refrigeration system using methanol as the working fluid. Int. J. Energy Res. 25, 115–128.

Roe, P., 1981. Approximate rieman solvers, parameters vectors, and difference schemes. J. Comput. Phys. 43, 357–372.

Roe, P., 1986. Characteristic based schemes for the euler equation. Annu. Rev. Fluid Mech. 18, 337–365.

Roshke, E.J., Massier, F.P., Gier, H.L., 1962. Experimental investigation of exhaust diffuser for rocket engines. Technical Report 32-210, Jet Propulsion Laboratory, Pasadena.

Sun, D.W., Eames, I.W., 1995. Recent development in the design theories and applications of ejector—a review. J. Inst. Energy 68, 65–79.

Wang, J.J., Chen, F., 1996. On the start condition of a second-throat ejector–diffuser. Aeronaut. J. 10, 321–326.

Wilcox, D., 1988. Reassessment of the scale determining equation for advanced turbulence models. AIAA J. 26 (11), 1299–1310.

Wilcox, D., 1994. Turbulence Modeling for CFD. DCW Industries, Inc., Griffin Printing, Glendale, California.

Zhou, B, Fleck, B.A., Bouak, F., Gauthier, J.E.D., 2000. Comparison of turbulence models for swirling effects on ejector performances. 8th Annual Conference of the CFD Society of Canada, vol. 1, Montreal, Canada, pp. 321–327.